

## Original article

# Pore-scale microfluidic investigation of unsaturated CO<sub>2</sub> bubble morphology and interface evolution during drainage-imbibition cycles

Ruirui Xue<sup>1,2</sup>, Yanran Chang<sup>1</sup>, Sijia Wang<sup>3</sup>, Pengfei Wang<sup>2</sup>\*, Huiru Sun<sup>4</sup>, Hantao Liu<sup>1</sup>, Pengfei Lv<sup>1</sup>✉\*

<sup>1</sup>School of Energy and Power Engineering, North University of China, Taiyuan 030051, P. R. China

<sup>2</sup>Advanced Institute for Ocean Research & Shenzhen Key Laboratory of Natural Gas Hydrates, Southern University of Science and Technology, Shenzhen 518055, P. R. China

<sup>3</sup>School of Energy and Environmental Engineering, Hebei University of Technology, Tianjin 11300401, P. R. China

<sup>4</sup>Department of Civil and Environmental Engineering, Monash University, Building 60, Melbourne, VIC 3800, Australia

### Keywords:

Bubble morphology  
interface evolution  
two-phase flow  
remobilization

### Cited as:

Xue, R., Chang, Y., Wang, S., Wang, P., Sun, H., Liu, H., Lv, P. Pore-scale microfluidic investigation of unsaturated CO<sub>2</sub> bubble morphology and interface evolution during drainage-imbibition cycles. *Capillarity*, 2025, 15(3): 74-86. <https://doi.org/10.46690/capi.2025.06.03>

### Abstract:

CO<sub>2</sub> sequestration into saline aquifers can significantly reduce atmospheric greenhouse gas concentrations, making it a key geological carbon storage technology for mitigating climate change and achieving carbon neutrality targets. However, current research predominantly focuses on reservoir saturation states, with limited understanding of dynamic mechanisms at the gas-liquid interface. In this study, microfluidic experiments were conducted at ambient temperature to investigate CO<sub>2</sub> drainage and imbibition under varying capillary numbers, incorporating the remobilization process driven by gas-water interphase mass transfer. Collectively, these three processes determine the temporal distribution of CO<sub>2</sub> and water phase saturations within the porous medium, thereby influencing the efficiency and long-term stability of CO<sub>2</sub> sequestration. With the increase of the capillary number, the sweep efficiency of CO<sub>2</sub> during drainage showed an upward trend, increasing to 54.71%. Moreover, this study provides an in-depth analysis of the distribution and morphological evolution of CO<sub>2</sub> under conditions where the aqueous phase is unsaturated. Results indicate that the asynchronous contraction of cluster interfaces results in a heterogeneous and dynamic dissolution process; the gas-water interface evolution of double-pore ganglia resembles the brine snap-off process; and singlet structures undergo shrinkage and deformation during the dissolution process. These findings elucidate the complex interactions between CO<sub>2</sub>-water in porous media and underscore the critical roles of capillary forces and interfacial dynamics in geological carbon sequestration.

## 1. Introduction

The widespread use of fossil fuels continues to drive economic growth and societal development, but it has also led to severe environmental challenges. Extensive consumption of fossil fuels has resulted in substantial emissions of greenhouse

gases, intensifying global climate change and triggering a series of ecological crises (Shukla et al., 2011). Over recent decades, carbon capture and storage in saline aquifers has been recognized as one of the most promising strategies to mitigate greenhouse gas emissions, owing to its vast storage

capacity and widespread geographic distribution (Celia, 2017). Consequently, an increasing number of countries and regions have made significant investments in the development of carbon capture and storage projects.

The CO<sub>2</sub> sequestration process in porous media involves two critical stages: drainage and imbibition. During drainage, CO<sub>2</sub>, as the non-wetting phase, is injected into porous media and displaces the resident water under a pressure gradient (Herring et al., 2013), with the CO<sub>2</sub>-brine interface advancing through successive Haines jumps (Wang et al., 2025). In contrast, imbibition occurs when injection ceases or environmental conditions change, allowing water to re-enter the pore spaces under capillary forces, partially replacing CO<sub>2</sub> and trapping it in small pores (Zhang et al., 2014). Generally, drainage dominates during the injection phase, while imbibition becomes significant in the post-injection stage (Lv et al., 2020). However, when the flow rate exceeds a critical capillary number, previously immobilized CO<sub>2</sub> can be remobilized, also known as remobilization (Guo et al., 2022). Prior studies have consistently demonstrated that the critical capillary number for CO<sub>2</sub> remobilization is typically required to surpass  $10^{-5}$  (Armstrong et al., 2014), enabling viscous forces to overcome capillary forces and mobilize isolated CO<sub>2</sub> bubble. Notably, these investigations were mainly based on water-saturated conditions, which do not completely represent the actual subsurface environment, where the aqueous phase may be fully saturated, partially saturated, or even unsaturated with CO<sub>2</sub>.

Moreover, the dissolution of CO<sub>2</sub> ganglion was reported to depend on the pore structure and multiphase distribution, and the existence of heterogeneity leads to localized mass transfer (Chen et al., 2018). Some pore size phenomena such as snap-off (double ganglia breaks into singlet) have been explored in previous studies, and the interaction between capillarity and mass transfer during CO<sub>2</sub> dissolution was determined with the model (Sahloul et al., 2002). Furthermore, the capillary pinning phenomenon (hindered the migration of CO<sub>2</sub>) can be caused by capillary pressure hysteresis, which has a positive effect on CO<sub>2</sub> sequestration (Zhao et al., 2014). However, most of these numerical models require experimental data for both validation and gaining insight into the complex pore-scale interactions (Kim et al., 2013).

Recently, microfluidic technology has emerged as a powerful tool for studying fluid flow behaviors in porous media due to its ability to achieve precise control and real-time visualization (Akamine et al., 2024). Microfluidic techniques have found extensive application in subsurface energy research, encompassing areas such as groundwater contamination, petroleum engineering, and multiphase flow phenomena (Porter et al., 2015; Xu et al., 2017; Rabbani et al., 2018; Jamshidi et al., 2019).

A classic phase diagram originally summarized by Lenormand et al. (1988) have divide the displacement patterns into capillary fingering, viscous fingering and stable displacement. Thereafter, the range of flow conditions have been expanded to supplement displacement mechanisms in some experimental researches (Wang et al., 2013; Jiang et al., 2018; Song et al., 2020). The behavior of fingering patterns is governed

by the capillary number (Ca), with CO<sub>2</sub> saturation initially decreasing in the capillary fingering regime and then increasing in the viscous fingering regime. There was a lot of CO<sub>2</sub> ganglia in the presence of inertia when Ca was higher, which increased capillary-correlation interface (Li et al., 2019). Song et al. (2020) further investigated CO<sub>2</sub>-brine displacement mechanisms in microfluidic devices with circular and square cross-sections, finding that the square cross-section yielded significantly higher CO<sub>2</sub> saturations due to changes in the tortuosity and wettability. Additionally, injection rate and salinity jointly influenced the displacement pattern and storage efficiency by modulating the balance between capillary and viscous forces.

The spatial distribution of two-phase flow in porous media is primarily dictated by the balance between capillary, viscous, and gravitational forces, whose relative magnitudes shape the observed flow regimes (Lee and Efendiev, 2018). According to the adjustable visualization equipment with more mature microfluidic technology, the overall flow of the two-phase fluid and the dynamic change of several pores have been well realized in recent years. Most investigations to date have focused on factors influencing CO<sub>2</sub> storage capacity prior to breakthrough. However, two-phase flow behavior at the pore scale after CO<sub>2</sub> breakthrough has been rarely explored. Additionally, most existing experiments have been conducted under ambient temperature and pressure in horizontal systems, whereas actual geological storage conditions typically involve high temperature and pressure, and pronounced gravitational effects. Han et al. (2016) experimentally demonstrated that gravity segregation plays a critical role in enhancing both oil recovery and CO<sub>2</sub> storage efficiency under immiscible conditions. Similarly, Rezk et al. (2019) conducted a series of core flooding tests under reservoir conditions and found that gravitational effects markedly improve performance in vertical reservoirs, proposing new dimensionless correlations for predicting outcomes during near-miscible CO<sub>2</sub> flooding. These findings highlight the necessity for future research to integrate actual geological conditions, combining numerical simulations and experimental validations to optimize displacement strategies.

In this study, microfluidic experiments were performed to investigate CO<sub>2</sub>-water displacement at ambient temperature under various capillary numbers. Pore-scale observations were used to elucidate the underlying mechanisms of drainage, imbibition, and remobilization, with particular emphasis on conditions where the aqueous phase is unsaturated with CO<sub>2</sub>. Additionally, the spatial distribution and morphological evolution of CO<sub>2</sub> were systematically analyzed, providing theoretical support for improving storage efficiency in saline aquifers.

## 2. Material and methods

### 2.1 Materials and apparatus

The experimental apparatus designed for the CO<sub>2</sub> drainage process under reservoir conditions (the pressure ranged from 1 to 40 bar and the temperature was 25 °C) is schematically

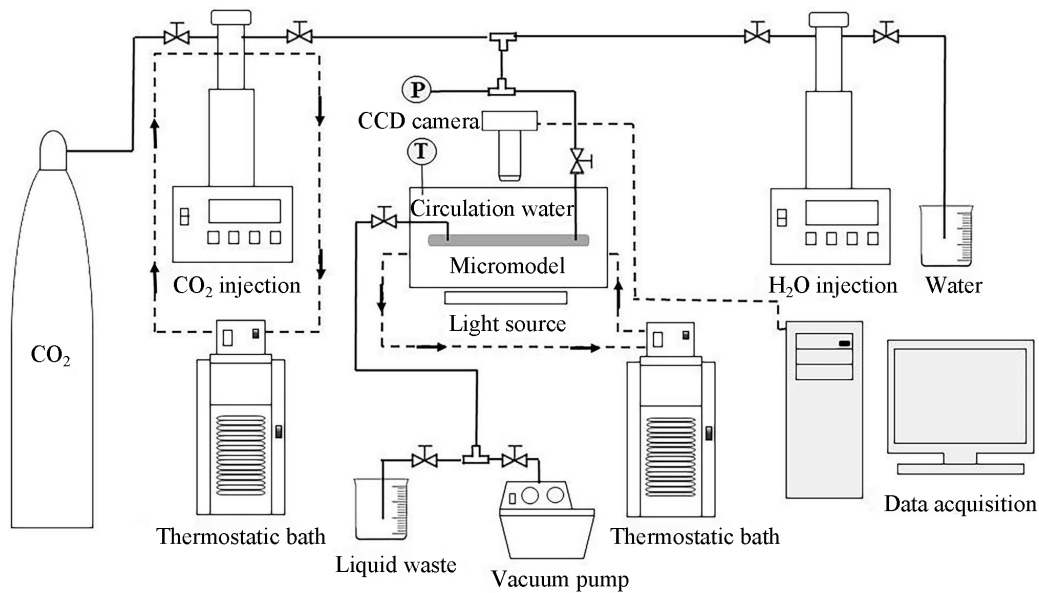


**Fig. 1.** Schematic diagram of experimental apparatus.

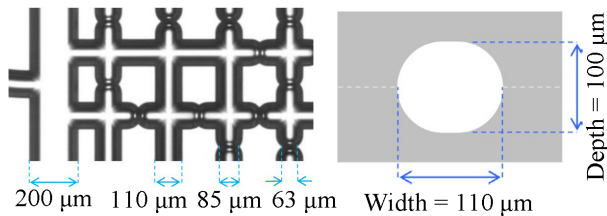


**Fig. 2.** Detailed information of the micromodel: Size of local pores and throats (left) and a typical symmetric channel profile on the chip (right).

illustrated in Fig. 1. The system comprises five primary components: a high-pressure micromodel system, temperature control system, imaging system, injection system, and vacuum extraction equipment. The micromodel was placed in the sink with circulating water, a thermostatic bath was used to control the system temperature. In this experimental setup, two ISCO pumps (260D, Teledyne Isco, USA) were utilized—one connected to a CO<sub>2</sub> cylinder for gas injection, and the other used to inject water and serve as a backpressure pump for pressure regulation. A vacuum pump was employed to evacuate residual air from the microfluidic chip prior to each test. The temperature sensor connected to the pipeline was used to detect temperature data during the process. Imaging was conducted using an optical microscope equipped with a charge-coupled device camera, with continuous video recording. In all experiments, CO<sub>2</sub> with a purity of 99.9% and deionized water were used as the displacing and displaced phases, respectively.

The micromodel serves as the central component of the experimental system. The glass micromodels used in this study were fabricated by Dolomite Centre Ltd. The high-pressure micromodel system consists of a porous media chip made of sodium-calcium glass and high-pressure connectors. This model can withstand the pressure difference (inside relative outside) of approximately 10 MPa, eliminating the need for

complex confining pressure devices. The porous area of the chip has a footprint of 10 × 60 mm<sup>2</sup>. Some details of the chip parameters are listed in the Fig. 2, with the chip dimensions being 90 × 15 mm<sup>2</sup> and the porous area 60 × 15 mm<sup>2</sup>. The Pore Volume (PV) is approximately 38 μL, and the permeability is estimated to be 80 Da. The channels in the grid have constrictions distributed randomly to mimic a naturally occurring rock structure. Due to the nearly axisymmetric nature of the chip's channels, the model pore network in this analysis uses a 2.5D micro-model, which has been shown to better represent multiphase flow in porous media (Avenidaño et al., 2019; Chang et al., 2020; Du et al., 2020). Specifically, three types of channels are randomly distributed to form the square structure: straight channels of 110 μm (Type I), constricted channels of 85 μm (Type II), and 63 μm (Type III). These three types of channels are randomly distributed to form a square-lattice structure.

## 2.2 Procedure

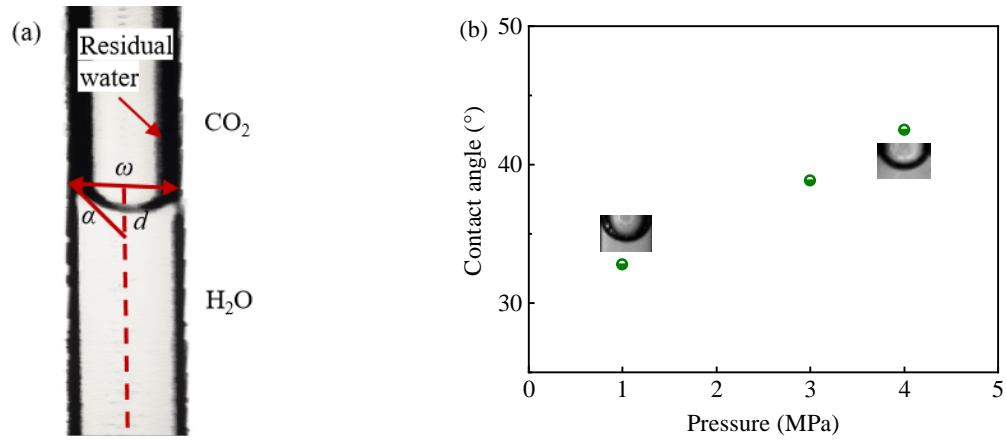
Experiments were conducted at an injection rate of 0.01 mL/min by systematically varying log Ca from -8.45 to -8.30 under pressures of 1, 3, and 4 MPa at a constant temperature of 25 °C. The capillary number (Ca) was calculated using Eq. (1):

$$Ca = \frac{Q\mu}{A\gamma} \quad (1)$$

where  $Q$  is the CO<sub>2</sub> injection rate (m<sup>3</sup>/s),  $\mu$  is the viscosity of water (Pa·s),  $A$  is the cross-sectional area of the porous medium (m<sup>2</sup>), determined by dividing the PV by the length of the porous domain, and  $\gamma$  is the interfacial tension between CO<sub>2</sub> and water (mN/m). The fluid properties and details of the log Ca calculations are summarized in Table 1 (Georgiadis et al., 2010; Al-Zaidi et al., 2019). This study focuses on the pore-scale behavior of gaseous CO<sub>2</sub> under the given conditions.

**Table 1.** Thermophysical properties of water and CO<sub>2</sub> at 25 °C under varying pressures.

Pressure (MPa)	Density (kg/m <sup>3</sup> )		Viscosity (Pa·s)		Interfacial tension (mN/m)	
	Water	CO <sub>2</sub>	Water	CO <sub>2</sub>	Water	CO <sub>2</sub>
1	997.49	18.73	$0.89 \times 10^{-3}$	$1.50 \times 10^{-5}$	65.73 ± 0.27	
3	998.39	64.15	$0.89 \times 10^{-3}$	$1.55 \times 10^{-5}$	52.42 ± 0.36	
4	998.84	93.47	$0.89 \times 10^{-3}$	$1.59 \times 10^{-5}$	47.02 ± 0.32	

**Fig. 3.** (a) Schematic diagram of contact angle measurement setup (microtube diameter: 100 μm) and (b) variation of contact angle with pressure at 1, 3 and 4 MPa.

Contact angle measurements were performed under experimental conditions, confirming that the untreated porous medium is hydrophilic. The specific measurement method is illustrated in Fig. 3. The contact angle is determined through digital image processing of experimental data, as detailed in Fig. 3(a). The calculation follows Eq. (2). Fig. 3(b) presents the trend of contact angle variation under different test pressures. The data points show a gradual increase in contact angle with increasing pressure, which subsequently influences the displacement process:

$$\alpha = \tan^{-1} \frac{\omega}{2d} \quad (2)$$

where  $\alpha$  is the contact angle (°),  $\omega$  signifies the throat width (mm), and  $d$  denotes the vertical distance at a particular position. The formula calculates the contact angle  $\alpha$  by taking the arctangent of the ratio of the throat width  $\omega$  to the vertical distance  $d$ .

The micromodel experiment mainly includes the following procedures:

- 1) **Micromodel Cleaning:** The micromodel was first filled with 100 PVs of ethanol. A vacuum pump was then activated to evacuate the system for 1 h, ensuring complete removal of residual liquids. Subsequently, 100 PVs of N<sub>2</sub> were injected to thoroughly dry the micromodel.
- 2) **Water Saturation:** Deionized water, unsaturated with CO<sub>2</sub>, was continuously injected into the micromodel at the target pressure and ambient temperature to ensure full saturation. A microscope was used to monitor the pro-

cess, and saturation was confirmed when no gas bubbles remained in the pore space.

- 3) **Drainage:** At the test pressure, CO<sub>2</sub> was injected into the water-saturated micromodel using an ISCO pump at a constant flow rate of 0.01 mL/min. Once the CO<sub>2</sub> phase reached the field of view, continuous image acquisition was initiated. Injection continued until no further phase changes were observed and the CO<sub>2</sub> distribution stabilized over time, indicating the end of the displacement process.
- 4) **Imbibition:** In this stage, water was injected from the opposite direction of the drainage flow to displace the residual CO<sub>2</sub>, enabling observation of capillary trapping and remobilization. Deionized water was injected at a constant volumetric rate until CO<sub>2</sub> was completely removed from the pore network. The gas-water two-phase flow was observed for quite a long time (more than 12 h after CO<sub>2</sub> breakthrough) in this study.
- 5) **Dynamic Imaging:** An integrated imaging and data acquisition system was used to capture the initial water distribution and continuously record the movement of the CO<sub>2</sub> displacement front throughout the entire experiment.

### 3. Results and discussion

#### 3.1 Displacement and dissolution mechanism

Optical images of CO<sub>2</sub> distribution with a long-term observation before and after CO<sub>2</sub> breakthrough in the pore network (for the representative log Ca) are shown in Figs.

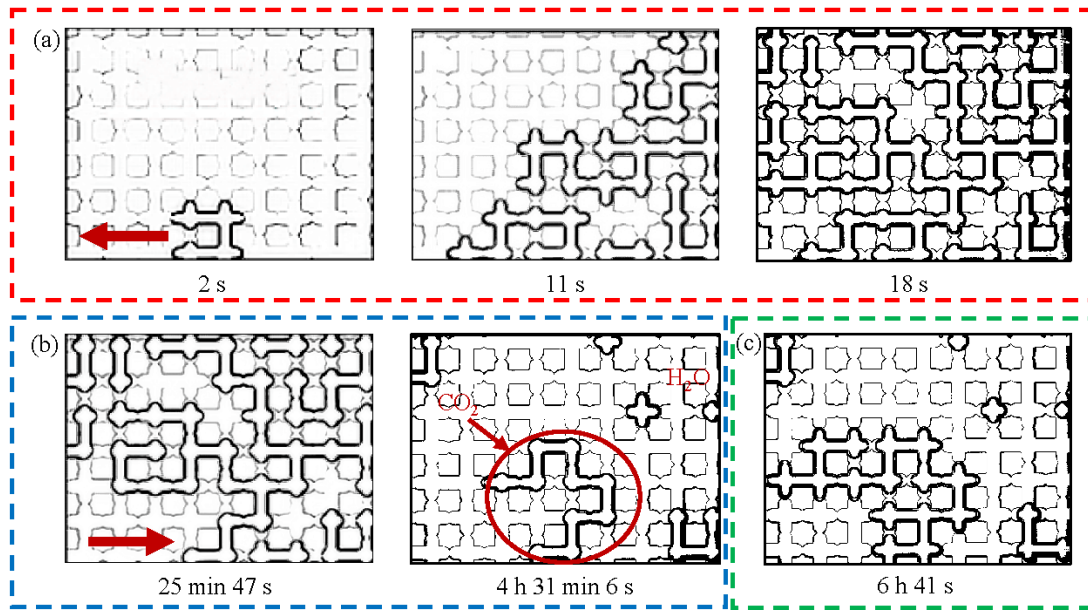


**Fig. 4.** CO<sub>2</sub>-water distributions observed over time at  $\log Ca = -8.45$  (0.01 mL/min under 1 MPa) during (a) drainage, (b) imbibition and (c) remobilization stages. The injection direction during the remobilization stage is the same as that in the imbibition stage.

4-6. These figures also indicate the corresponding time for each observation stage. To enhance the contrast between the two phases, the invading CO<sub>2</sub> was represented by the black contours.

Upon completion of the displacement process within the micromodel, a portion of the CO<sub>2</sub> typically remains undissolved in the aqueous phase. Nevertheless, subsequent long-term observations indicate that the gas-aqueous phase distribution does not remain static. This dynamic behavior is hypothesized to originate primarily from localized pore-scale processes driven by cyclic mechanisms involving drainage, imbibition, and remobilization (Herring et al., 2021). Such mechanisms could potentially enhance subsequent CO<sub>2</sub> trapping, thereby influencing the overall long-term geological sequestration (Ahn et al., 2020).

As depicted in Fig. 4(a), during the drainage stage at 1 MPa and before CO<sub>2</sub> breakthrough, the injected CO<sub>2</sub>, driven by the applied pressure, displaces the water (the wetting phase) into adjacent pore regions. The interaction between localized capillary and inertial forces triggers rapid fluid rearrangements, commonly observed as Haines jumps. The flow pattern of CO<sub>2</sub> is primarily influenced by the pore geometry and fluid properties, often resulting in intricate migration pathways. At the microscale, CO<sub>2</sub> can appear as either a continuous phase or discrete ganglia, gradually displacing the aqueous phase and causing it to become segmented and encapsulated within the pore network. Macroscopically, this process is observed as water flowing toward the outlet, while CO<sub>2</sub> accumulates near the injection zone.

After the CO<sub>2</sub> breakthrough, the water phase (wetting phase), driven predominantly by capillary forces, begins to invade pore throats. This process, known as imbibition, segments the previously continuous CO<sub>2</sub> phase into isolated ganglia or

droplets. During imbibition, water films develop and thicken along the pore walls, facilitating the re-entry of water into pore spaces formerly occupied by CO<sub>2</sub>, as illustrated in Fig. 4(b). As imbibition advances, isolated water structures may merge, leading to the entrapment of CO<sub>2</sub> portions as disconnected bubbles or ganglia within the pore network. Concurrently, the dissolution rate of these trapped CO<sub>2</sub> entities can accelerate, inducing morphological changes, particularly noted for structures identified as clusters and ganglia (Moghadasi et al., 2023). Even under constant pressure conditions, the evolving morphology and connectivity of the trapped CO<sub>2</sub> phase can significantly influence the long-term security of CO<sub>2</sub> geological storage.

Due to the potential unsaturation of the water phase, mass transfer alters the local capillary forces, leading to the remobilization of CO<sub>2</sub> bubbles. Changes in flow conditions can release previously trapped CO<sub>2</sub> from the porous matrix, allowing it to merge with neighboring bubbles, reconnect into a continuous phase, and reduce interfacial area. The remobilized CO<sub>2</sub> subsequently migrates through the pore channels, displacing the surrounding water and leading to localized increases in CO<sub>2</sub> saturation, as illustrated in Fig. 4(c). The observed rise in saturation indicates that gas-liquid mass transfer during imbibition can trigger remobilization of isolated CO<sub>2</sub> bubbles even at capillary numbers significantly lower than the critical threshold ( $Ca^*$ ).

Under the 3 MPa condition, the overall characteristics of the drainage and imbibition processes resemble those observed at 1 MPa, as illustrated in Fig. 5. However, it is noteworthy that during the drainage, particularly within the region highlighted by the green circle in Fig. 5(a), the CO<sub>2</sub> flow path manifests as continuous and relatively uniform. This behavior is attributed to the experimental condition where capillary forces appear

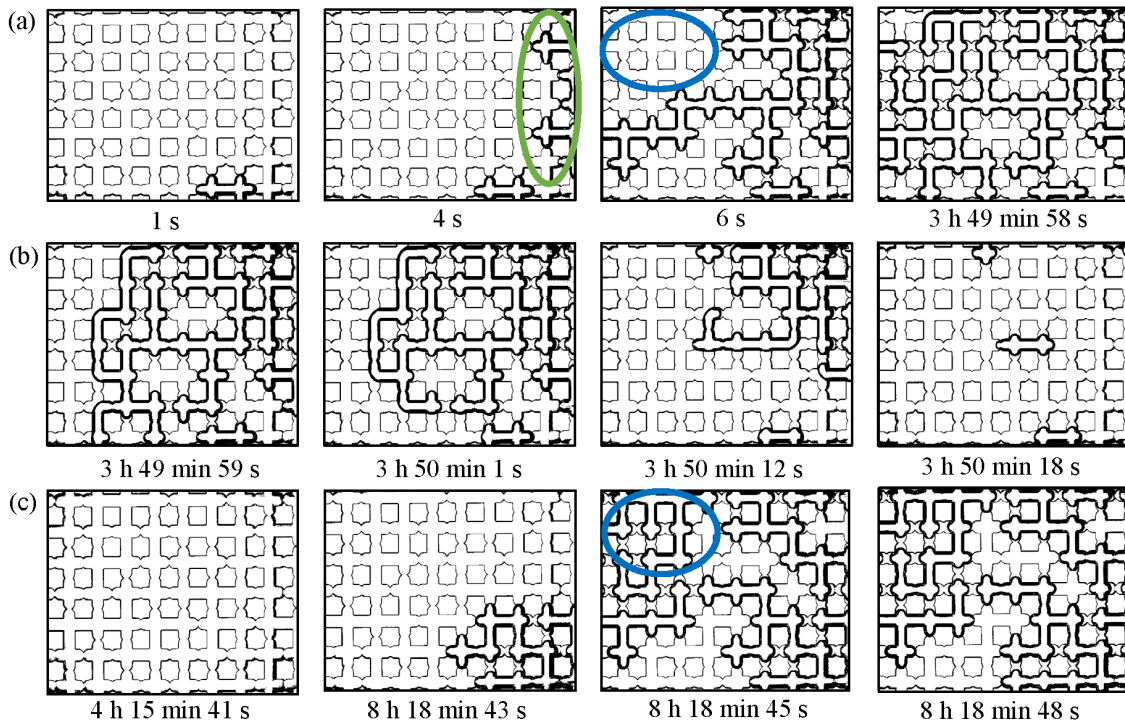


**Fig. 5.** CO<sub>2</sub>-water distributions observed over time at  $\log Ca = -8.35$  (0.01 mL/min under 3 MPa) during (a) drainage, (b) imbibition and (c) remobilization stages.

insufficient to promote significant fingering phenomenon, consequently leading to a smoother interface morphology and a more uniform advancement of the CO<sub>2</sub>-water front through the porous media.

The remobilization process under the 3 MPa condition is depicted in Fig. 5(c). While the overall connectivity and distribution patterns of CO<sub>2</sub> during the drainage and remobilization phases exhibit similarities, distinct differences are observed, particularly within the region highlighted by the blue circle. During drainage, the CO<sub>2</sub> flow path primarily advances from the injection point towards the outlet. Conversely, during remobilization, previously trapped CO<sub>2</sub> is released from its original locations and redistributed, forming new and potentially irregular flow pathways. This distinction arises partly because drainage is typically characterized by relatively unidirectional flow leading to a progressive increase in CO<sub>2</sub> saturation from the inlet. In contrast, remobilization can be intermittent and involves the redistribution of CO<sub>2</sub> across various pore spaces throughout the medium.

As illustrated in Fig. 6(a), during the drainage process conducted at 4 MPa, within the region delineated by the orange circle, the advancing CO<sub>2</sub> front exhibits a finger-like or tongue-like morphology. This front progressively invades the space initially occupied by water, displacing it into pore corners or smaller adjacent pores. The emergence of this pattern is attributed to the further increase in pressure, which enhances viscous forces relative to capillary forces. Although  $Ca$  rises slightly, it remains sufficiently low such that fingering begins to develop, establishing preferential flow paths (Qin et al., 2025). These fingering structures typically manifest in zones characterized by higher porosity or superior connectiv-

ity. Similar to the observations at lower pressures, the overall CO<sub>2</sub> connectivity and distribution patterns during drainage and remobilization share general similarities (Fig. 6). Nevertheless, distinct differences are apparent during remobilization, particularly in the area highlighted by the blue circle, compared to the distribution observed near the inlet during the initial drainage phase.

As the injection pressure was elevated from 3 to 4 MPa, the time required to achieve breakthrough decreased from 3 h 49 min to 3 h 9 min. This observation indicates that, under a constant injection rate, a higher driving pressure enhances the displacement efficiency of CO<sub>2</sub>, resulting in a shorter breakthrough time and consequently, a more rapid occupation of the available PV. Moreover, wettability (represented by the contact angle) also influences the displacement rate. Under 4 MPa conditions, the larger contact angle allows the non-wetting phase to more easily occupy the pore spaces, thereby driving the expulsion of the wetting phase.

Furthermore, the mode and extent of CO<sub>2</sub> displacement during the initial drainage phase significantly influence the characteristics of the subsequent imbibition process. As detailed in Table 2, an increase of  $\log Ca$  from -8.45 to -8.30 corresponds to an enhancement in the CO<sub>2</sub> sweep efficiency during drainage, rising from 47.32% to 54.71%. This more effective displacement occupies a larger fraction of the PV, resulting in a more fragmented and disconnected residual aqueous phase (Cai et al., 2021). Consequently, during the subsequent imbibition phase (illustrated in Fig. 6), the pathways available for water re-entry become substantially more tortuous. For example, as  $\log Ca$  increases from -8.35 to -8.30, the characteristic time required for imbibition extends

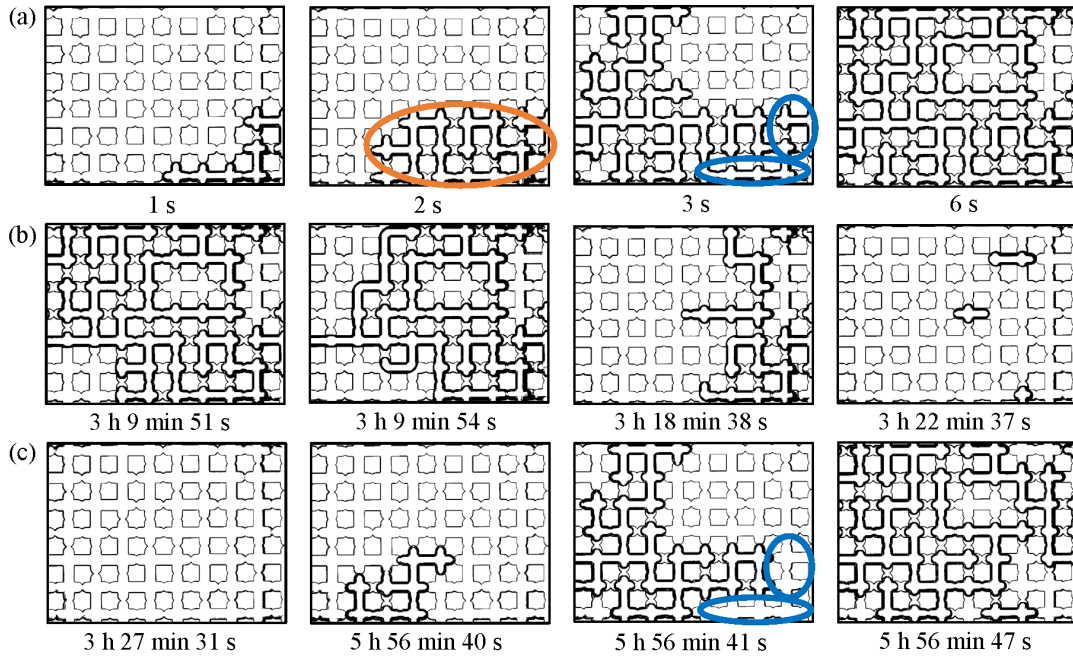


**Fig. 6.** CO<sub>2</sub>-water distributions observed over time at  $\log Ca = -8.30$  (0.01 mL/min under 4 MPa) during (a) drainage, (b) imbibition and (c) remobilization stages.

**Table 2.** Sweep efficiency evolution with time under varied capillary numbers.

Regime	$\log Ca = -8.45$		$\log Ca = -8.35$		$\log Ca = -8.30$	
	$t$ (s)	Sweep efficiency (%)	$t$ (s)	Sweep efficiency (%)	$t$ (s)	Sweep efficiency (%)
Drainage	2	3.94	1	2.16	1	7.44
	11	32.12	4	8.06	2	18.23
	18	47.32	6	34.59	3	40.29
	/	/	13,798	52.52	6	54.71
Imbibition	1,547	41.92	13799	42.59	11,391	51.45
	16,266	17.31	13,801	39.03	11,394	40.29
	/	/	13,812	21.97	11,918	19.63
	/	/	13,818	5.01	12,157	3.39
Remobilization	21,641	24.83	15,341	0	12,451	0
	/	/	29,923	12.37	21,400	9.26
	/	/	29,925	48	21,401	32.26
	/	/	29,928	49.39	21,407	51.26

significantly, rising from approximately 19 s to 12 min 46 s due to the increased tortuosity of re-entry pathways. In line with this retardation, the sweep efficiency during imbibition also exhibits a decrease, declining from 5.01% to 3.39%, indicating a less effective water redistribution due to the hindered connectivity of flow paths. This observed prolongation of the imbibition duration may also be partially attributed to alterations in wettability; specifically, an increase in the contact angle as pressure elevates from 3 to 4 MPa. Such a change

would diminish the affinity between the water phase and the surface, thereby reducing the propensity for spontaneous water imbibition into the pore network. It has been noted that the imbibition process exhibits greater sensitivity to wettability alterations compared to the primary drainage phase (Hu et al., 2017). Ultimately, the wettability characteristics of the CO<sub>2</sub>-water system exert a critical influence on the efficacy and long-term security of CO<sub>2</sub> geological storage (Zhang et al., 2025).

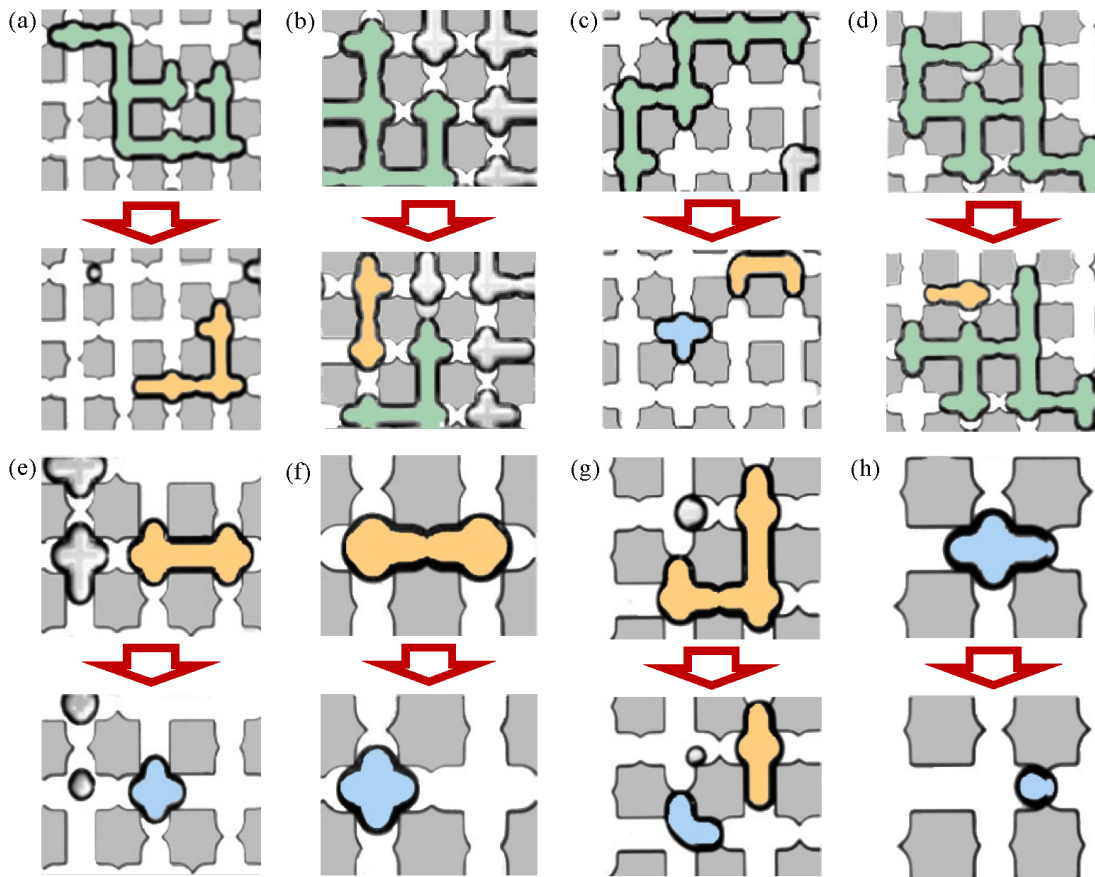


**Fig. 7.** Two dimensional images of eight representative interface evolution regions after breakthrough of the CO<sub>2</sub>-water interface. CO<sub>2</sub> structures are categorized into clusters (green), ganglia (yellow), and singlets (blue) based on their connectivity and size. The following demonstration indicates the interfacial area: (a) Clusters shrinking into ganglia, (b) and (c) cluster fragmentation, (d) ganglia detaching from cluster, (e) and (g) ganglia fragmentation, (f) ganglia shrinking into singlet and (h) singlet shrinking to singlet.

Concurrently, the characteristics of water films, droplets, and the specific configurations of CO<sub>2</sub> entrapment established during imbibition significantly influence the subsequent remobilization process. Specifically, if imbibition results in the formation of numerous isolated CO<sub>2</sub> ganglia enveloped by water, their subsequent mobilization during the remobilization phase may be impeded, necessitating a greater driving force to induce coalescence and flow. Furthermore, the heterogeneity of the intra-pore fluid distribution established during imbibition inherently affects the resultant flow pathways and velocities during remobilization. A comparison between Figs. 5(b) and 6(b) reveals a more dispersed CO<sub>2</sub> phase distribution in the latter, characterized by a higher prevalence of isolated CO<sub>2</sub> ganglia. This increased fragmentation contributes to a slight decline in remobilization sweep efficiency, decreasing from 51.26% to 49.39%. Consequently, the efficiency of CO<sub>2</sub> recovery during remobilization is adversely affected by capillary barriers and limited phase connectivity resulting from the fluid configuration established during the preceding imbibition process.

### 3.2 CO<sub>2</sub> distribution and morphology

#### 3.2.1 CO<sub>2</sub> bubble evolution

As CO<sub>2</sub> dissolves into the water phase, the interfacial area between the CO<sub>2</sub> and water phases progressively diminishes. During this mass transfer process, the dissolution of carbon dioxide into water induces alterations in both the interfacial area and the interface morphology. These modifications are coupled and collectively dictate the ultimate configuration of the interface. Fig. 7 presents two-dimensional images capturing the evolution of eight representative regions of the CO<sub>2</sub>-water interface after breakthrough. A comparison with the three-dimensional visualizations of the CO<sub>2</sub>-brine interface presented by Jiang et al. (2019) highlights notable parallels in the interfacial dynamics observed in both studies.

In the investigation of CO<sub>2</sub>-water interface evolution, the interfaces are categorized into three distinct types: clusters, ganglia, and singlets. A cluster is defined as a continuous or semi-continuous CO<sub>2</sub>-water interface occupying multiple interconnected pores within the porous medium. Typically composed of several adjacent interfacial regions, clusters possess the largest interfacial area among the types but are relatively few in number. During the initial stages, clusters dominate the mass transfer process due to their substantial

interfacial area, which significantly facilitates CO<sub>2</sub> dissolution. As the experiment progresses, clusters tend to shrink or fragment into smaller entities, namely ganglia. Ganglia typically reside within one to three pores. Their evolution is complex, characterized by relatively regular shapes but significant dynamic changes, including contraction, fragmentation, or persistent trapping. Ganglia commonly originate from the breakup of larger clusters or through localized dissolution events occurring at pore throats. Singlets are generally confined to individual pores, exhibiting irregular shapes and possessing the smallest interfacial area. They often manifest as discrete bubbles situated in pore corners or throats. The dissolution rate of singlets is comparatively slow, primarily constrained by the reduced mass transfer efficiency associated with their limited interfacial area. These distinct interface types exhibit differential evolutionary characteristics during CO<sub>2</sub> dissolution, profoundly impacting both mass transfer dynamics and overall interfacial stability.

Brine invades the CO<sub>2</sub> phase primarily through mechanisms of bypass flow and snap-off (Lebedeva and Fogden, 2011). Bypass flow tends to govern the formation and persistence of larger clusters, whereas snap-off events lead to the disconnection of CO<sub>2</sub> filaments at pore throats, thereby generating smaller ganglia (Liu et al., 2022). The reduction in cluster size can occur via three principal mechanisms. Firstly, as depicted in Fig. 7(a), in-situ shrinkage occurs at the cluster periphery upon water invasion, causing portions of the cluster to contract into smaller entities. This process is driven by the large interfacial area exposed to water and the significant concentration gradient between the CO<sub>2</sub> phase and the surrounding water. This high concentration difference provides a strong driving force for mass transfer, promoting rapid CO<sub>2</sub> dissolution into the water phase and consequently reducing the cluster's interfacial area (Patmonoaji and Suekane, 2017). Secondly, water preferentially invades larger pores, gradually displacing the CO<sub>2</sub>. Concurrently, CO<sub>2</sub> at the cluster margins dissolves into the water via mass transfer, leading to the contraction of the cluster, potentially forming ganglia. Thirdly, clusters can undergo fragmentation into smaller ganglia or clusters, as illustrated in Figs. 7(b) and 7(c). This fragmentation can be induced when advancing water rapidly bypasses connected CO<sub>2</sub> residing in larger pores (often characterized by high aspect ratios) via networks of smaller pores. The resulting pressure differential across the cluster can lead to its breakup into discrete residual ganglia and smaller clusters within the pore bodies (Pak et al., 2015). Furthermore, detachment of ganglia from larger clusters can occur due to water invasion and displacement forces, as shown in Fig. 7(d). As water flows through pore throats, it can exert hydrodynamic forces on the connecting necks between ganglia and the parent cluster, causing the ganglia to detach and become independent interfacial regions. Under sufficient pressure gradients, clusters may also fracture at narrow, connecting pore throats, breaking into multiple smaller segments.

Although ganglia are comparatively smaller entities, they can nonetheless undergo fragmentation under specific circumstances, as exemplified in Figs. 7(e) and 7(g). However, given that ganglia typically occupy only one to three pores, the

likelihood of such fragmentation is generally lower compared to clusters. Fragmentation may occur when there is a non-uniform pressure distribution within the pore space or when the hydrodynamic drag forces exerted by the flowing aqueous phase on the ganglion surpass a critical threshold (Wang and Xu, 2024). Alternatively, ganglia may undergo shrinkage, diminishing in size to form smaller singlets, as illustrated in Fig. 7(f). This reduction in volume is primarily driven by the continuous dissolution of CO<sub>2</sub> into the surrounding water phase. Furthermore, if a ganglion exhibits an irregular morphology or possesses a tenuous connection across a pore throat, the increased accessibility of the CO<sub>2</sub> surface to water can accelerate dissolution, promoting its contraction into smaller, singlet-like structures.

Regarding singlets, while their evolution in size and shape exhibits stochastic variations, they generally undergo progressive shrinkage over time, as depicted in Fig. 7(h). This diminution is attributed to the continuous dissolution of CO<sub>2</sub> into the surrounding aqueous phase, thereby reducing the volume of CO<sub>2</sub> comprising the singlet. These observations suggest that the long-term persistence of singlets can impair mass transfer efficiency, potentially prolonging the overall timescale required for effective CO<sub>2</sub> sequestration.

### 3.2.2 Interface evolution of singlet

As depicted in Fig. 8, during the dissolution process of a singlet, both its volume and interfacial area diminish, potentially causing it to regress from occupying a single pore structure to becoming a smaller, discrete bubble within that pore. The rate of dissolution at the surface of a CO<sub>2</sub> singlet during imbibition can exhibit spatial variations attributable to differences in local concentration gradients, fluid flow velocities, and the specific pore geometry. Analogous to the influence of bedding direction observed in shale imbibition, the morphological evolution of CO<sub>2</sub> bubbles may be modulated by the anisotropy of the porous medium (Fu et al., 2024). Furthermore, alterations in wettability exert a profound influence on both the morphology of CO<sub>2</sub> bubbles and the dynamics of interface evolution (Alhammad et al., 2024; Pryazhnikov et al., 2024).

A singlet, being confined within an individual pore, is characterized by an interface predominantly consisting of the gas-water boundary, exhibiting minimal contact area with the pore wall. Local concentration gradients can arise across the singlet surface due to spatial variations in fluid flow patterns and dissolution kinetics. These gradients influence the overall dissolution rate and can lead to anisotropic interface recession, whereby the rate of shrinkage differs across various portions of the singlet surface, consequently causing deformation or non-uniform contraction. During the dissolution process, mass transfer between the singlet and the surrounding aqueous phase represents the critical limiting step (Qin et al., 2024). This mass transfer typically proceeds via a combination of diffusion, the inherent migration of solute molecules from regions of higher concentration to lower concentration, and convection, which involves mass transport facilitated by bulk fluid movement (Patmonoaji and Suekane, 2017). Additionally, variations in capillary pressure or interfacial tension across the

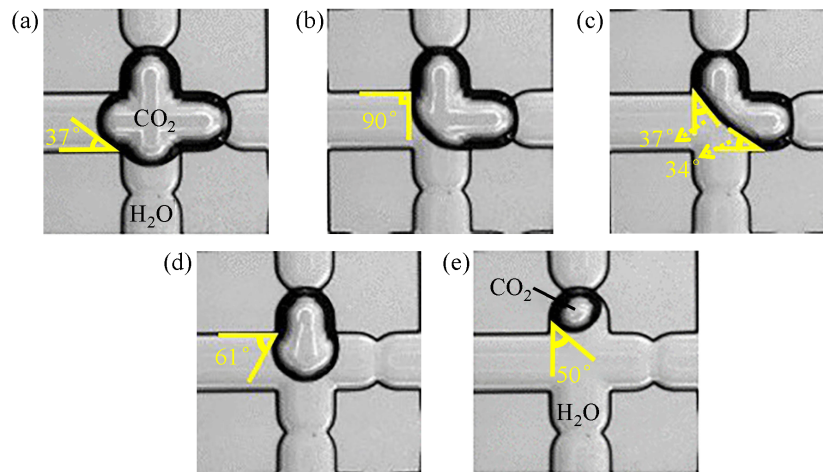


**Fig. 8.** Snapshots of the dissolution history of a singlet: (a)-(c) The initial singlet contraction process and (d)-(e) the subsequent degenerative contraction to a smaller singlet.

singlet's curved interface can induce localized stress differences. These stresses may contribute to the deformation of the singlet in specific regions, thereby influencing the dynamics of interfacial recession (Yang et al., 2020). Concurrently, the morphological changes induced by this anisotropic interfacial recession can, in turn, influence the subsequent dissolution kinetics and overall stability of the gas phase. Experimental investigation of these dynamics is crucial for developing a comprehensive understanding of the phenomenon and provides a theoretical basis for optimizing CO<sub>2</sub> displacement processes involving water injection.

As depicted in Fig. 8(a), the initial stage is characterized by the presence of CO<sub>2</sub> as isolated bubbles (singlets), exhibiting high interfacial curvature. Dissolution commences as the singlet peripheries establish contact with the surrounding water phase. Owing to the small volume of singlets, the gas-water interface (specifically, the meniscus interface) constitutes a substantial proportion of the total surface area. This configuration provides numerous sites for dissolution and ensures extensive contact with the wetting phase. The meniscus interface is considered the primary determinant of mass transfer rates. For singlets, the ratio between meniscus interfacial area and total interfacial area is initially high and tends to increase as the bubble volume diminishes (Hu et al., 2020). Consequently, the significant relative area of the meniscus interface facilitates an elevated dissolution rate and rapid shrinkage. Because the peripheral regions maintain more extensive contact with the brine, their local dissolution rate is comparatively faster, resulting in interfacial recession that proceeds inwards from the edges and causes a rapid decrease in the singlet radius.

As dissolution progresses, the volume of the singlet diminishes. Within pore corners, the contact line may become pinned due to geometric constraints, potentially leading to an apparent increase in the contact angle, possibly approaching 90° (Ma et al., 1996). Concurrently, owing to ongoing mass transfer, the reduction in the gas-water interfacial area leads to a decrease in the local capillary forces and a diminished

concentration gradient across the interface. This results in a lower dissolution rate and a reduced driving force for mass transfer, as illustrated in Fig. 8(b). Under these conditions, the relative contribution of convection to the overall dissolution process may become more pronounced. With continued CO<sub>2</sub> dissolution, the bubble volume contracts further, prompting a readjustment of the interfacial curvature. In a hydrophilic medium, this readjustment typically involves the aqueous phase re-establishing contact with the solid surface previously occupied by the CO<sub>2</sub>, leading to the restoration of a lower equilibrium contact angle, as depicted in Fig. 8(c).

In the terminal stages, the singlet may diminish substantially in size, potentially leading to its complete disappearance. The ratio of the gas-water interfacial area to the total interfacial area continues to increase, signifying greater exposure of the active gas-water interface and an enlarged contact area between the singlet and the wetting phase. This geometric configuration consequently accelerates the dissolution process. The overall dissolution rate remains primarily governed by the available interfacial area until complete dissolution is achieved, as illustrated in Fig. 8(e). During this final phase, the dissolution dynamics are strongly influenced by the interplay between surface tension effects and local fluid flow conditions, potentially approaching a dynamic equilibrium between dissolution and transport processes.

#### 4. Conclusions

The interplay between drainage, imbibition, and remobilization processes collectively dictates the spatio-temporal saturation distribution of CO<sub>2</sub> and aqueous phases within the porous medium, thereby influencing both the efficiency and long-term stability of CO<sub>2</sub> sequestration.

At a constant flow rate, higher injection pressures enhance the displacement capability of CO<sub>2</sub>, resulting in shorter breakthrough times. Under drainage conditions at 3 MPa, the CO<sub>2</sub> flow path tends to be continuous and relatively uniform. However, at 4 MPa, increased viscous forces promote the development of fingering, causing CO<sub>2</sub> to advance in finger-

like morphologies. Furthermore, the displacement pattern and extent achieved during drainage significantly impact the subsequent imbibition phase. As  $\log Ca$  increases from -8.45 to -8.30, the sweep efficiency of  $CO_2$  during drainage improves from 47.32% to 54.71%. This leads to a more fragmented distribution of the displaced aqueous phase. Consequently, during the subsequent imbibition phase, the pathways for water imbibition become more tortuous, extending the imbibition time by approximately 40-fold. The formation of water films, droplets, and the specific configurations of  $CO_2$  entrapment during imbibition subsequently influence the potential for remobilization.

Within porous media, the dynamics of the  $CO_2$ -water interface represent a complex process. Due to mass transfer, the dissolution of  $CO_2$  into water alters the interfacial area and simultaneously induces changes in interfacial morphology. These processes are interdependent and collectively determine the final configuration of the interface.

Specifically, during the dissolution of a singlet, its volume and interfacial area progressively decrease. Notably, the ratio of meniscus interfacial area to total interfacial area, which is initially high for singlets, tends to increase further as the bubble volume decreases. A larger relative gas-water interfacial area facilitates a higher dissolution rate, leading to more rapid contraction. Investigating these interfacial dynamics enhances the understanding of  $CO_2$  behavior within porous media, thereby enabling the optimization of storage and extraction strategies and improving overall resource utilization efficiency.

This study was conducted using a micromodel with a relatively uniform pore size distribution and idealized pore geometries, which do not fully represent the complexity and heterogeneity of natural geological formations. The larger and more regular pore structures used in this study, while beneficial for direct visualization and experimental control, represent a geometric simplification that may limit the direct applicability of our conclusions to natural subsurface environments. Future work should consider extending the analysis to more representative porous media, such as natural rock samples or micro-CT-based three-dimensional pore networks, to further validate and generalize the observed mechanisms under more realistic subsurface conditions.

## Acknowledgements

This study was supported by the National Natural Science Foundation of China (Nos. 52106213 and 52406071), Shanxi Scholarship Council of China (2024-115), Shanxi Province Graduate Research Innovation Project (No. 2024KY625), Key Talent Team for Science and Technology Innovation in Shanxi Province (No. 202204051002023), and Shenzhen Science and Technology Program (No. JCYJ20220818095605012).

## Conflict of interest

The authors declare no competing interest.

**Open Access** This article is distributed under the terms and conditions of the Creative Commons Attribution (CC BY-NC-ND) license, which permits unrestricted use, distribution, and reproduction in any medium, provided the original work is properly cited.

## References

- Ahn, H., Kim, S. O., Lee, M., et al. Migration and residual trapping of immiscible fluids during cyclic injection: Pore-scale observation and quantitative analysis. *Geofluids*, 2020, 2020: 4569208.
- Akamine, T., Tosuai, T., Ramadhan, R., et al. Visualizing oil displacement by nanofluids at pore scale: A concentration-dependent nanofluid spreading induced by structural disjoining pressure. *Capillarity*, 2024, 12(1): 17-26.
- Alhammad, F., Ali, M., Yekeen, N., et al. The influence of methyl orange on the  $CO_2$ -brine wettability of organic-acid-aged calcite samples: Implications for  $CO_2$  geostorage. *Advances in Geo-Energy Research*, 2024, 12(2): 102-112.
- Al-Zaidi, E., Edlmann, K., Fan, X. Gaseous  $CO_2$  behaviour during water displacement in a sandstone core sample. *International Journal of Greenhouse Gas Control*, 2019, 80: 32-42.
- Armstrong, R. T., Georgiadis, A., Ott, H., et al. Critical capillary number: Desaturation studied with fast X-ray computed microtomography. *Geophysical Research Letters*, 2014, 41(1): 55-60.
- Avendaño, J., Lima, N., Quevedo, A., et al. Effect of surface wettability on immiscible displacement in a microfluidic porous media. *Energies*, 2019, 12(4): 664.
- Cai, J., Jin, T., Kou, J., et al. Lucas-Washburn equation-based modeling of capillary-driven flow in porous systems. *Langmuir*, 2021, 37(5): 1623-1636.
- Celia, M. A. Geological storage of captured carbon dioxide as a large-scale carbon mitigation option. *Water Resources Research*, 2017, 53(5): 3527-3533.
- Chang, C., Kneafsey, T. J., Wan, J., et al. Impacts of mixed-wettability on brine drainage and supercritical  $CO_2$  storage efficiency in a 2.5-D heterogeneous micromodel. *Water Resources Research*, 2020, 56(7): e2019WR026789.
- Chen, L., Wang, M., Kang, Q., et al. Pore scale study of multiphase multicomponent reactive transport during  $CO_2$  dissolution trapping. *Advances in Water Resources*, 2018, 116: 208-218.
- Du, Y., Mehmani, A., Xu, K., et al. Microfluidic diagnostics of the impact of local microfracture connectivity on hydrocarbon recovery following water injection. *Water Resources Research*, 2020, 56(7): e2019WR026944.
- Fu, C., Xu, X., Du, Y., et al. Experimental study on the influence of pore structure on spontaneous imbibition in marine black shale. *Capillarity*, 2024, 10(3): 57-72.
- Georgiadis, A., Maitland, G., Trusler, J. P. M., et al. Interfacial tension measurements of the ( $H_2O + CO_2$ ) system at elevated pressures and temperatures. *Journal of Chemical & Engineering Data*, 2010, 55(10): 4168-4175.
- Guo, H., Song, K., Hilfer, R. A brief review of capillary number and its use in capillary desaturation curves. *Transport in Porous Media*, 2022, 144(1): 3-31.
- Han, J., Lee, M., Lee, W., et al. Effect of gravity segregation on  $CO_2$  sequestration and oil production during  $CO_2$  flooding. *Applied Energy*, 2016, 161: 85-91.

- Herring, A. L., Harper, E. J., Andersson, L., et al. Effect of fluid topology on residual nonwetting phase trapping: Implications for geologic CO<sub>2</sub> sequestration. *Advances in Water Resources*, 2013, 62: 47-58.
- Herring, A. L., Sun, C., Armstrong, R. T., et al. Evolution of bentheimer sandstone wettability during cyclic scCO<sub>2</sub>-brine injections. *Water Resources Research*, 2021, 57(11): e2021WR030891.
- Hu, R., Wan, J., Kim, Y., et al. Wettability impact on supercritical CO<sub>2</sub> capillary trapping: Pore-scale visualization and quantification. *Water Resources Research*, 2017, 53(8): 6377-6394.
- Hu, Y., She, Y., Patmonoaji, A., et al. Effect of capillary number on morphological characterizations of trapped gas bubbles: Study by using micro-tomography. *International Journal of Heat and Mass Transfer*, 2020, 163: 120508.
- Jamshidi, T., Zeng, F., Tontiwachwuthikul, P., et al. Viability of carbonated water injection (CWI) as a means of secondary oil recovery in heavy oil systems in presence and absence of wormholes: Microfluidic experiments. *Fuel*, 2019, 249: 286-293.
- Jiang, L., Wang, S., Li, X., et al. The role of flow rates on flow patterns and saturation in high-permeability porous media. *International Journal of Greenhouse Gas Control*, 2018, 78: 364-374.
- Jiang, L., Wu, B., Liu, Y., et al. Dynamic evolution of the CO<sub>2</sub>-brine interfacial area during brine imbibition in porous media. *International Journal of Heat and Mass Transfer*, 2019, 128: 1125-1135.
- Kim, M., Sell, A., Sinton, D. Aquifer-on-a-Chip: Understanding pore-scale salt precipitation dynamics during CO<sub>2</sub> sequestration. *Lab on a Chip*, 2013, 13(13): 2508-2518.
- Lebedeva, E. V., Fogden, A. Micro-CT and wettability analysis of oil recovery from sand packs and the effect of waterflood salinity and kaolinite. *Energy & Fuels*, 2011, 25(12): 5683-5694.
- Lee, S. H., Efendiev, Y. Hybrid discretization of multi-phase flow in porous media in the presence of viscous, gravitational, and capillary forces. *Computational Geosciences*, 2018, 22(5): 1403-1421.
- Lenormand, R., Touboul, E., Zarcone, C. Numerical models and experiments on immiscible displacements in porous media. *Journal of Fluid Mechanics*, 1988, 189: 165-187.
- Liu, Y., Berg, S., Ju, Y., et al. Systematic investigation of corner flow impact in forced imbibition. *Water Resources Research*, 2022, 58(10): e2022WR032402.
- Li, Y., Blois, G., Kazemifar, F., et al. High-speed quantification of pore-scale multiphase flow of water and supercritical CO<sub>2</sub> in 2-D heterogeneous porous micromodels: Flow regimes and interface dynamics. *Water Resources Research*, 2019, 55(5): 3758-3779.
- Lv, P., Liu, Y., Yang, W. Investigation on CO<sub>2</sub> permeation in water-saturated porous media with disordered pore sizes. *Experimental Thermal and Fluid Science*, 2020, 119: 110207.
- Ma, S., Mason, G., Morrow, N. R. Effect of contact angle on drainage and imbibition in regular polygonal tubes. *Colloids and Surfaces A: Physicochemical and Engineering Aspects*, 1996, 117(3): 273-291.
- Moghadasli, R., Goodarzi, S., Zhang, Y. Pore-scale characterization of residual gas remobilization in CO<sub>2</sub> geological storage. *Advances in Water Resources*, 2023, 179: 104499.
- Pak, T., Butler, I. B., Geiger, S., et al. Droplet fragmentation: 3D imaging of a previously unidentified pore-scale process during multiphase flow in porous media. *Proceedings of the National Academy of Sciences of the United States of America*, 2015, 112(7): 1947-1952.
- Patmonoaji, A., Suekane, T. Investigation of CO<sub>2</sub> dissolution via mass transfer inside a porous medium. *Advances in Water Resources*, 2017, 110: 97-106.
- Porter, M. L., Jiménez-Martínez, J., Martínez, R., et al. Geomaterial microfluidics at reservoir conditions for subsurface energy resource applications. *Lab on a Chip*, 2015, 15(20): 4044-4053.
- Pryazhnikov, M. I., Zhigarev, V. A., Minakov, A. V., et al. Spontaneous imbibition experiments for enhanced oil recovery with silica nanosols. *Capillarity*, 2024, 10(3): 73-86.
- Qin, X., Wang, H., Xia, Y., et al. Micro- and nanoscale flow mechanisms in porous rocks based on pore-scale modeling. *Capillarity*, 2024, 13(1): 24-28.
- Qin, X., Wang, H., Xia, Y., et al. Pore-scale investigation of water-CO<sub>2</sub>-oil flow in shale fractures for enhanced displacement efficiency and CO<sub>2</sub> sequestration. *Engineering Geology*, 2025, 348: 107969.
- Rabbani, H. S., Or, D., Liu, Y., et al. Suppressing viscous fingering in structured porous media. *Proceedings of the National Academy of Sciences of the United States of America*, 2018, 115(19): 4833-4838.
- Rezk, M. G., Foroozesh, J., Zivar, D., et al. CO<sub>2</sub> storage potential during CO<sub>2</sub> enhanced oil recovery in sandstone reservoirs. *Journal of Natural Gas Science and Engineering*, 2019, 66: 233-243.
- Sahloul, N. A., Ioannidis, M. A., Chatzis, I. Dissolution of residual non-aqueous phase liquids in porous media: Pore-scale mechanisms and mass transfer rates. *Advances in Water Resources*, 2002, 25(1): 33-49.
- Shukla, R., Ranjith, P. G., Choi, S. K., et al. Study of caprock integrity in geosequestration of carbon dioxide. *International Journal of Geomechanics*, 2011, 11(4): 294-301.
- Song, Y., Zhao, C., Chen, M., et al. Pore-scale visualization study on CO<sub>2</sub> displacement of brine in micromodels with circular and square cross sections. *International Journal of Greenhouse Gas Control*, 2020, 95: 102958.
- Wang, C., Xu, K. Ganglion startup in porous media. *Chemical Engineering Science*, 2024, 292: 119982.
- Wang, Y., Zhang, C., Wei, N., et al. Experimental study of crossover from capillary to viscous fingering for supercritical CO<sub>2</sub>-water displacement in a homogeneous pore network. *Environmental Science & Technology*, 2013, 47(1): 212-218.
- Wang, Z., Sun, R., Gan, Y., et al. Controlled Haines jumps in a dual-channel multiphase system: Inferring fluid properties from the dynamics of interface motion. *Journal of*

- Fluid Mechanics, 2025, 1002: A40.
- Xu, K., Liang, T., Zhu, P., et al. A 2.5-D glass micromodel for investigation of multi-phase flow in porous media. *Lab on a Chip*, 2017, 17(4): 640-646.
- Yang, Y., Li, Y., Yao, J., et al. Dynamic pore-scale dissolution by CO<sub>2</sub>-saturated brine in carbonates: Impact of homogeneous versus fractured versus vuggy pore structure. *Water Resources Research*, 2020, 56(4): e2019WR026112.
- Zhang, H., Mahmoud, M., Iglauer, S., et al. Field-scale investigation of CO<sub>2</sub> plume dynamics under spatial wettability variations: Implications for geological CO<sub>2</sub> storage. *Advances in Geo-Energy Research*, 2025, 15(3): 230-244.
- Zhang, Y., Nishizawa, O., Kiyama, T., et al. Flow behaviour of supercritical CO<sub>2</sub> and brine in Berea sandstone during drainage and imbibition revealed by medical X-ray CT images. *Geophysical Journal International*, 2014, 197(3): 1789-1807.
- Zhao, B., MacMinn, C. W., Huppert, H. E., et al. Capillary pinning and blunting of immiscible gravity currents in porous media. *Water Resources Research*, 2014, 50(9): 7067-7081.